Climate Dynamics (2025) 63:43
https://doi.org/10.1007/s00382-024-07544-0

ORIGINAL ARTICLE

The reversal of surface wind speed trend in Northeast China: impact from aerosol emissions

Haozeyu Miao[1,2,3] · Haiming Xu[1,2] · Kai Yang[3,6] · Haosu Tang[8] · Jiechun Deng[1,2] · Meng Xu[9] · Guicai Ning[7] · Gang Huang[3,4,5]

Received: 27 August 2024 / Accepted: 3 December 2024
© The Author(s), under exclusive licence to Springer-Verlag GmbH Germany, part of Springer Nature 2024

Abstract
A "stilling" or "reversal" of surface wind speed (SWS) trend over the landmass of the Northern Hemisphere has been observed during the past decades, with notable regional disparities. In particular, the reversal of SWS in Northeast China is observed in 2010, which is different to the features over other regions such as North China (reversal in 2006), South China (reversal in 2000), and East China (no reversal). However, the mechanism behind the unique feature of SWS reversal over Northeast China is inadequately understood. Although previous studies generally attributed the reversal of SWS trend to large-scale ocean–atmosphere circulation (LOAC) signals, here we show that the interdecadal decline in local aerosols measured by aerosol optical depth (AOD) also contributes to the reversal of SWS over Northeast China, supported by the results from a sensitivity experiment conducted using Community Atmosphere Model version (CAM) 5.3 and the Detection and Attribution Model Intercomparison Project (DAMIP). Specifically, the aerosol reduction acts to decrease low-level static stability and enhance turbulent kinetic energy (TKE), increasing local SWS. Quantitative analyses indicate that the anthropogenic aerosol reduction plays a dominant role in the observed increasing SWS in the recent decade. Our results emphasize the importance of considering aerosol changes for a comprehensive understanding of SWS changes on regional scales.

Keywords Wind speed reversal · Aerosol · Northeast China · CAM5.3 · CMIP6 · Attribution

1 Introduction

Surface wind speed (SWS) is a crucial parameter for atmospheric dynamics, and its changes are closely linked to land–atmosphere interactions and regional climate change. SWS can affect evaporation processes, which in turn affect ground-air heat and water vapor fluxes, thereby exerting a significant impact on weather and climate (McVicar et al. 2012). In addition, SWS also establishes a meteorological condition for the air pollutant dispersion, thereby influencing

✉ Haiming Xu
hxu@nuist.edu.cn

✉ Gang Huang
hg@mail.iap.ac.cn

[1] Key Laboratory of Meteorological Disaster (KLME), Ministry of Education & Collaborative Innovation Center On Forecast and Evaluation of Meteorological Disasters (CIC-FEMD), Nanjing University of Information Science & Technology, Nanjing 210044, China

[2] School of Atmospheric Sciences, Nanjing University of Information Science & Technology, Nanjing 210044, China

[3] State Key Laboratory of Numerical Modeling for Atmospheric Sciences and Geophysical Fluid Dynamics, Institute of Atmospheric Physics, Chinese Academy of Sciences, Beijing 100029, China

[4] Laboratory for Regional Oceanography and Numerical Modeling, Qingdao National Laboratory for Marine Science and Technology, Qingdao 266237, China

[5] University of Chinese Academy of Sciences, Beijing 100049, China

[6] Center for Southern Hemisphere Oceans Research, Commonwealth Scientific and Industrial Research Organisation (CSIRO) Oceans and Atmosphere, Hobart 7004, Australia

[7] School of Atmospheric Physics, Nanjing University of Information Science & Technology, Nanjing 210044, China

[8] Department of Geography, University of Sheffield, Sheffield, UK

[9] School of Artificial Intelligence and Computer Science, Nantong University, Nantong, China

Published online: 17 December 2024

air quality (Paulot et al. 2022). More importantly, wind energy production can also be quantified by SWS. Wind energy is one of the most important clear energy resources under the goals toward reducing the emissions of greenhouse gas (GHG) and mitigating the global warming. Specifically, wind energy is proportional to the cube of the wind speed, and 1%–5% reductions in SWS will lead to wind energy losses of 2%–9% (Jacobson and Kaufman 2006).

Under the background of global warming, the global SWS has been generally decreased over land of the Northern Hemisphere, known as the SWS "stilling" (Tian et al. 2019; Vautard et al. 2010). Particularly, the SWS decline is also reported in China, which is the largest market of global wind energy (Guo et al. 2011; Lin et al. 2013). The weakening of SWS is not only related to the internal variability associated with atmospheric circulation, but also comes from the impact of human activities such as land use and land cover change (LUCC), and anthropogenic aerosols. For example, Xu et al. (2006) suggested that the decreasing SWS over China from 1969 to 2000 was due to the steady decline in the East Asian monsoon. Based on the observation minus reanalysis (OMR) method, Zha et al. (2017) quantified the effects of LUCC on SWS and found that LUCC can account for a downward trend of -0.12 m s^{-1} per decade in SWS in China over the last 30 years. Li et al. (2018) mainly attributed the surface wind declining to changes in underlying surfaces induced by urbanization in East China. As an important atmosphere component, aerosols can induce global and regional climate responses in different ways. Previous studies indicated that the variation of aerosol optical depth (AOD) had significant influences on various near-surface meteorological variables, such as vegetation and precipitation (Li et al. 2011; Tariq et al. 2022). In terms of aerosol impact on SWS, Jacobson and Kaufman (2006) suggested that aerosol particles may weaken the short-term SWS in California by stabilizing the atmosphere. Bichet et al. (2012) reported a decline of -0.3 m s^{-1} in global terrestrial SWS from 1975 to 2005, which is related to the increasing aerosol emissions based on sensitivity experiments.

Despite the generally decreasing SWS trend, several studies have reported SWS reversal over land of the Northern Hemisphere during the past decade (Zeng et al. 2019; Zha et al. 2021b). However, notable disparities exist in the reversal timing of SWS trend due to the use of different datasets, regions, and periods. For example, the SWS reversals in North America, Europe, and Asia occurred in 2012, 2003, and 2001, respectively (Zeng et al. 2019). Zhang and Wang (2020) divided the SWS trends in China from 1960 to 2017 into three periods, and found a near-zero annual trend from 1960 to 1969, a prominent decrease of -0.24 m s^{-1} per decade from 1970 to 2004, and a weak reversal from 2005 to 2017. Till now, the investigate of SWS reversal focuses on large area such as eastern China, which is a power load center and an important region for wind power development (Li et al. 2022; Zha et al. 2021b). They found that the SWS changes can be related to the combined effects of variations in multiple large-scale ocean–atmosphere circulation (LOAC) signals, such as the Pacific Decadal Oscillation (PDO), North Atlantic oscillation (NAO), Arctic Oscillation (AO), and and El Niño-Southern Oscillation (ENSO). By refining the SWS changes in eastern China into smaller regions, we show that the characteristic of SWS reversal over Northeast China differs from that in the other regions of eastern China (Fig. 1). The years with the shift from the weakening to strengthening of annual mean SWS are around 2010, 2006 and 2000 in Northeast China, North China and South China, respectively, while the terrestrial stilling is continuously ongoing in East China.

Different SWS reversal features underscore the presence of distinct factors controlling the SWS trend in each area. Figure 1 shows that AOD has simultaneous reversals in the year of 2010 in four regions of eastern China, but only the SWS in Northeast China also reversed in this year. This paper highlights the potential impact of recent aerosol reductions on the reversal of SWS over Northeast China in 2010, which may fill research gaps and deepen our understanding of regional long-term SWS variation. The remainder of the paper is structured as follows. In Sect. 2, we describe the datasets and methods used in this study. In Sect. 3, we explore the observed evolution of SWS in Northeast China and a possible mechanism behind this interdecadal change. Individual effect under different forcings and aerosol emission conditions from CAM5.3 and CMIP6 models are shown in Sect. 4. Conclusion and discussions are given in Sect. 5.

2 Data and methods

2.1 Data

2.1.1 SWS observations

We use daily SWS data observed from ground weather stations from 1980 to 2020 to calculate monthly averaged SWS field across China. The stations are carefully selected from the National Meteorological Information Center (NMIC) of the China Meteorological Administration (CMA) database based on strict quality control procedures, such as the temporal consistency test, homogeneity test, and extreme test. We use the Pettitt test (Pettitt 1979) to remove stations that were moved from one place to a distant other place, only retaining the stations with less than 0.02° (about 2 km) in horizontal relocation and less than 20 m in vertical relocation. To reduce the impact of missing value, we remove stations in which missing data account for more than 1% of the total time series. Thus, 157 stations with continuous

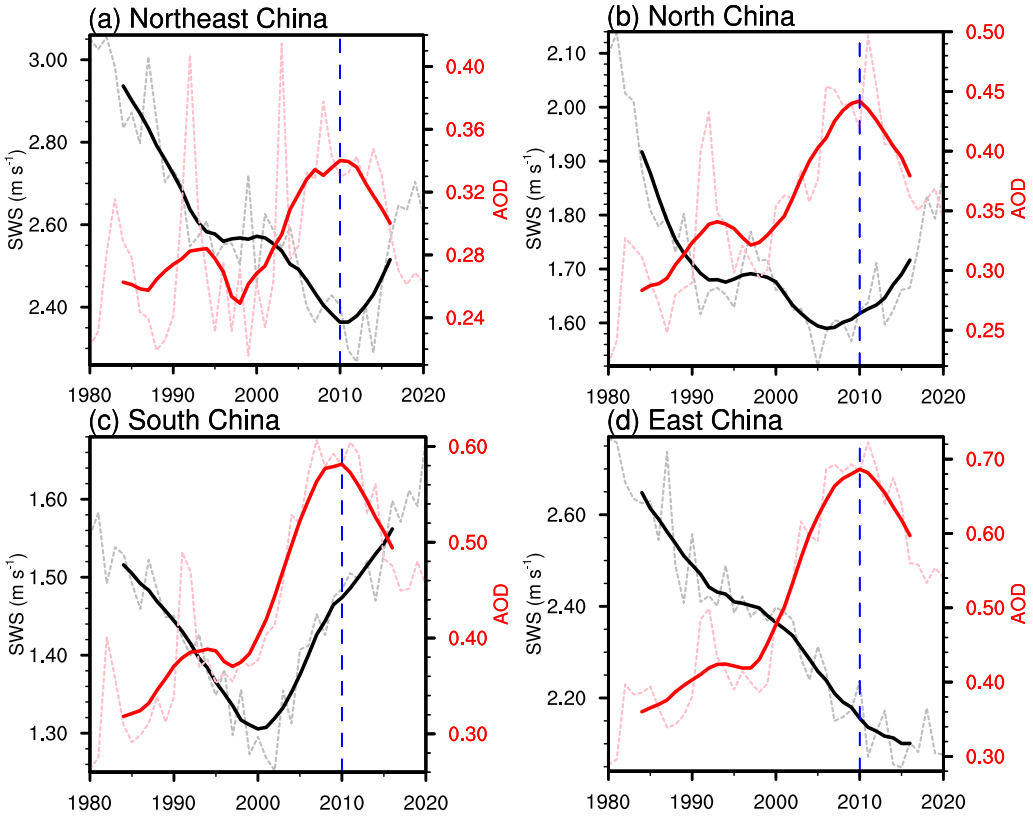

Fig. 1 Time series of raw (light dashed curve) and 9-year Gaussian low-pass filtered (heavy solid curve) observed SWS (black; units: m s^{-1}) and AOD at 550 nm (red) in **a** Northeast China (38.5°N–54°N, 119.5°E–135°E), **b** North China (32°N–40°N, 105°E–115°E), **c** South China (22°N–32°N, 105°E–120°E), and **d** East China (32°N–40°N, 115°E–123°E) from 1980 to 2020. The vertical dashed blue line denotes the turning point of AOD in year 2010

monthly wind records in Northeast China (38.5°N–54°N, 119.5°E–135°E) are selected for the study period of 1980–2020 (Fig. S1). The definition of latitude and longitude range of Northeast China used is the same throughout the study. We also use another observational dataset to validate the result (Figs. S2 and S3). The stations are selected from the Global Summary of Day (GSOD) database quality-control checked by Zeng et al. (2019).

2.1.2 Reanalysis datasets

In this study, the monthly mean AOD at 550 nm is obtained from the Modern Era Retrospective analysis for Research and Applications Version 2 (MERRA-2; Gelaro et al. 2017) provided by the National Aeronautics and Space Administration (NASA).

Considering inherent limitations in reanalysis datasets, we compare observed SWS with those from four different reanalysis datasets, including the fifth generation European Centre for Medium-Range Weather Forecasts (ECMWF) reanalysis (ERA-5; Hersbach et al. 2020), the Japanese Meteorological Agency 55-Year Reanalysis (JRA-55; Kobayashi et al. 2015), the National Centers for Environmental Prediction (NCEP) Climate Forecast System Reanalysis (CFSR; Saha et al. 2010), and MERRA-2. Detailed information about the reanalysis datasets can be found in Table S1 in the supplementary material. All reanalysis datasets are widely used for climate change studies across China (Jiang et al. 2021; Miao et al. 2020; Su et al. 2015). All the data are calculated as the monthly averaged SWS for further comparison. In order to better compare the ability of reanalysis data reproducing the observed SWS features, we uniformly interpolate the gridded data of reanalysis to meteorological stations in Northeast China using bilinear interpolation (Miao et al. 2023). Four reanalysis datasets are evaluated to the observational dataset for the period of 1980–2020, when all the data are available.

2.1.3 CMIP6 model datasets

To validate SWS responses to the AOD variation, we also use model simulations from the Detection and Attribution Model Intercomparison Project (DAMIP; Gillett et al. 2016) in the Coupled Model Intercomparison Project Phase 6

(CMIP6). The DAMIP simulations are single-forcing experiments (with only one external forcing of interest varying over time and all other forcings fixed at the constant pre-industrial levels). The experiments used in this paper are hist-aer (with anthropogenic aerosol forcing only; referred to as AER), hist-GHG (with well-mixed GHG forcing only; referred to as GHG), and hist-nat (with natural forcing only; i.e., volcanic and solar activities; referred to as NAT). The selected variables include monthly near-surface wind speed, aerosol optical thickness at 550 nm, and air temperature from 1000 to 850 hPa with an interval of 75 hPa. We use eight models with the mentioned experiments and variables covering the historical period of 1900–2020, with three realizations used for each model. Multi-model ensemble (MME) means are used to determine which forcing factor is responsible for different responses in the historical experiments. The list of models included in each set of simulations can be found in Table S2 in the supplementary material. To facilitate inter-model comparison, all model outputs are remapped onto a $1^\circ \times 1^\circ$ grid using bilinear interpolation.

2.2 Methods

2.2.1 Definition of static stability

Atmospheric static stability measures the gravitational resistance of the atmosphere to vertical displacement, which reflects the characteristics of the atmosphere affecting the vertical motion. It is the result of a fundamental adjustment of buoyancy, and thus is determined by the vertical stratification of potential temperature or density. The static stability is calculated by the following equation (Bluestein 1992):

$$S = -\frac{T}{\theta} \times \frac{d\theta}{dP}$$

where T is the air temperature, θ is the potential temperature, and P is the pressure. The static stability influences the dynamics of various atmospheric motions including wind.

2.2.2 Statistical methods

For consistency, all variables cover the same study period of 1980–2020. The Mann–Kendall test for trend in Sen's slope estimate (Sen 1968) is used to detect trends in SWS and estimate trend magnitude and its significance. The method does not assume a particular distribution of the data and is not sensitive to outliers. This statistical significance test for trends may not be reliable for the highly auto-correlated time series. Fourier analysis and Gaussian filtering are performed to remove interannual variation (Schaefer and Domroes 2009; Moreira et al. 2015) with a focus on interdecadal variation.

2.2.3 CESM1 model description and experimental design

The Community Atmosphere Model Version 5.3 (CAM5.3; Neale et al. 2010) serves as the atmosphere component of the Community Earth System Model version 1.2.2 (CESM1.2.2), which is released by the National Center for Atmospheric Research (NCAR). CAM5.3 used in this study has a resolution of 1.9° at latitude and 2.5° at longitude and a hybrid vertical coordinate with 30 levels, including a rigid lid at 3.653 hPa. The model runs with prescribed climatological monthly mean sea surface temperature during 1982–2001.

To verify the impact of the AOD on the interdecadal SWS variation in the observations and further reveal the impact processes and mechanisms, one control experiment (CTRL) and five sensitivity experiments (EXP) are performed. Five EXP runs start with the initial fields on January 1 of the first year through the fifth year in CTRL, respectively. The average results of five EXP experiments are analyzed in order to limit the influence of internal variability. CTRL run is prescribed with anthropogenic aerosol emissions in the year of 2000, while EXP runs reduce anthropogenic aerosol emissions to one-tenth of those in CTRL at the surface or in the troposphere over Northeast China, and keep them same as CTRL in all other regions. All control and sensitivity runs are newly initialized runs. Since atmospheric responses to external forcings are fast, each experiment is integrated for 15 years, and the last 10 years of simulated data are analyzed. The model configuration and experiment setting have been similarly and widely used for investigating the East Asia climate in many previous researches (e.g., Deng and Xu 2015; Xu et al. 2022; Zhou et al. 2020).

2.2.4 Multiple linear regression model

To quantitatively decompose the contributions of external forcing factors to observed SWS changes, we construct a combined index using a multiple linear regression model, which is given by:

$$SWS_{OBS} = a \times SWS_{AER} + b \times SWS_{GHG} + c \times SWS_{NAT} + d$$

In this model, SWS_{OBS} denotes observed SWS change, SWS_{AER}, SWS_{GHG}, and SWS_{NAT} represent the contributions from aerosol, GHG, and natural forcings, respectively. The regression coefficients a, b, and c quantify the relative impacts of the respective forcing factors, and d represents the intercept term that captures any constant bias in the observational data. This approach allows us to effectively isolate individual effects of different forcing factors on the observed SWS change.

3 Observational and reanalysis results

3.1 Changes of observed SWS and AOD in MERRA-2 in Northeast China

Figure 1a shows the time series of the raw and interdecadal annual-mean SWS and AOD over Northeast China. Clearly, the interdecadal variations of SWS and AOD are highly anti-correlated with a correlation coefficient of about −0.80 ($P < 0.001$) based on an effective degree of freedom of 13.67. This result is also confirmed in another observational dataset (Fig. S3). The evolution of SWS and AOD in the GSOD observations is almost the same as that in the CMA observations, with an interdecadal correlation of SWS and AOD of −0.81 ($P < 0.001$). This indicates that higher SWS can be observed over Northeast China under lower aerosol emissions at interdecadal timescales. Simultaneously, the interdecadal trends of SWS and AOD are reversed around 2010, that is, a negative (or decreasing) SWS trend over Northeast China during 1980–2010 is significantly shifted to a positive (or increasing) trend after 2010, while the AOD shows the opposite trend reversal. Specifically, the SWS trend is −0.21 m s^{-1} per decade ($P < 0.001$) accompanied by an AOD trend of 0.02 per decade ($P < 0.05$) during 1980–2010, which is then reversed to 0.47 m s^{-1} per decade ($P < 0.01$) with an AOD trend of −0.09 per decade ($P < 0.05$) during 2010–2020. Notably, extreme AOD values in 1983, 1992, and 2003 are associated with the El Chichón and Mount Pinatubo volcanic eruptions, and Siberian forest fires, respectively (Gelaro et al. 2017). We replace the values for these three years with the average of the two years before and after the three years, respectively (Fig. S4). The results show a similar significant negative correlation between SWS and AOD in the Northeast China, with a correlation coefficient of −0.85 (Fig. S4a), which demonstrates that these extreme years have limited impact on our results. Thus, the effects of these extreme events on long-term changes in SWS are not taken into account in this study.

This is also true for the interdecadal evolutions of seasonal mean SWS with a similar transition from a negative to positive trend around year 2010 (Fig. S5). The interdecadal correlation coefficient between SWS and AOD for each season is −0.86 in spring ($P < 0.001$), −0.87 in summer ($P < 0.001$), −0.61 in autumn ($P < 0.05$), and −0.50 in winter ($P < 0.05$). However, we should note some seasonal differences in the interdecadal AOD evolution. The spring and summer mean AOD peaks in 2010 and declines thereafter, consistent with its annual mean. The AOD reversal timing lags slightly in autumn, but the trend shift is insignificant in winter. This is likely because anthropogenic aerosol emissions are concentrated in spring and summer, with lower values in autumn and winter. The climatological means of spring, summer, autumn, and winter AOD over Northeast China are 0.36, 0.35, 0.24, and 0.20, respectively. These results are consistent with previous findings that AOD over East China reaches its maximum in spring and its minimum in winter (He et al. 2012).

It should be noted that the significant reversal of the SWS trend averaged over Northeast China does not mean that it can be detected at all the stations used in this study, thus, this reversal can be likely dominated by a few stations with extremely strong interdecadal variations. To further confirm the widespread reversal of the SWS trend over Northeast China, we show spatial patterns of the SWS trends for 2000–2010 and 2010–2020 (Fig. 2a, b). It can be seen that 75.6% of the total stations (90 out of the 119 stations) display significant decreasing trends of annual-mean SWS ($P < 0.1$) before 2010 (Fig. 2a), while 96.2% of the total stations (102 out of the 106 stations) show increasing trends of annual-mean SWS ($P < 0.1$) after 2010 (Fig. 2b). The spatial contrast in AOD changes is more pronounced, with the increasing trend in the early period and the decreasing trend in the late period for almost all the stations (Fig. 2c, d).

The spatial trends of seasonal SWS are consistent, that is, 86.2%, 83.2%, 73.3%, and 61.7% of all the stations show decreasing trends in spring, summer, autumn, and winter from 2000 to 2010 at $P < 0.1$ level (Fig. 3). These percentages increase to 93.1%, 99.1%, 96.4%, and 91.0%, respectively, after 2010 at $P < 0.1$ level, indicating a robust reversal of the SWS trend in Northeast China. The spatial patterns of the seasonal AOD trends have higher consistency than those of SWS (Fig. 4). The AOD at almost all stations shows opposite trend changes in the periods before and after 2010, and the trends are significant at more stations at $P < 0.1$ level during the 2010–2020 period compared to the earlier period. In addition, the trends are larger in spring and summer than in the other seasons.

Since the evolutions of annual mean SWS and AOD show the main features of their intra-annual cycles, we will focus on the annual mean timescale next.

3.2 Potential mechanisms between SWS and AOD shifts

Before exploring the possible effects of AOD on SWS variation, we assess the capability of the reanalysis datasets in reproducing long-term changes in SWS trend (Fig. S6). Except for the ERA-5, all reanalysis datasets can reproduce the SWS reversal in Northeast China, although the SWS reversals in the CFSR and MERRA-2 lag slightly behind those in the observations. Note that the trend magnitudes of different reanalysis datasets differ, and all of them tend to underestimate the trends both before and after the turning point. Consistent with the finding of Miao et al. (2020) for

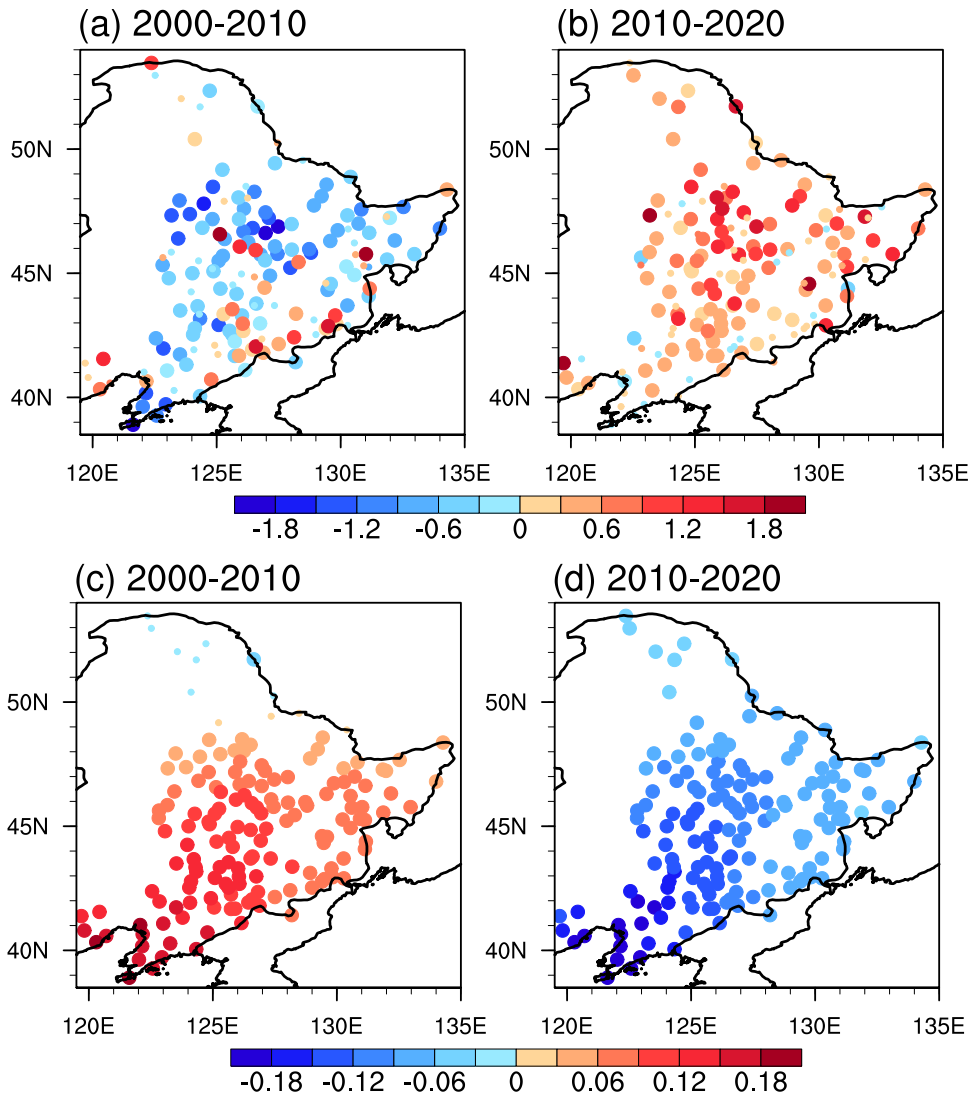

Fig. 2 Spatial patterns of linear trends in SWS (**a** and **b**; units: m s^{-1} per decade) and AOD (**c** and **d**; units: per decade) during the two periods of 2000–2010 (**a** and **c**) and 2010–2020 (**b** and **d**) are shown. Larger dots in **a**–**d** indicate the 90% confidence level (i.e., $P < 0.1$)

East Asia, the reanalysis datasets closest to the observations over Northeast China are the JRA-55 and CFSR, which are chosen for the subsequent analyses. Monthly mean air temperatures from the JRA-55 are used to compute the static stability, and monthly mean TKE from the CFSR is also used.

Aerosols interact strongly with meteorological variables within the planetary boundary layer (PBL) and bring about a range of climatic responses (Ding et al. 2016; Yu et al. 2002). By scattering and absorbing solar radiation, aerosols can induce temperature inversions, and the resulting strong contrast between surface cooling and upper PBL warming helps stabilize the PBL and attenuate turbulent mixing, thereby reducing SWS. Figure 5 shows the spatial patterns of meridionally averaged atmospheric static stability trends for the two periods before and after 2010, respectively. The trend of the upper-level PBL (above 925 hPa) during the early period is opposite to that of the lower-level PBL (below 925 hPa). This is mainly due to the distinct effects of aerosol absorption on the atmospheric stability of the upper and lower layers. The static stability generally increases below 925 hPa over Northeast China from 2000 to 2010 (Fig. 5a) as the meteorological stations in the region are mostly located below this level (Fig. S1), thus leading to a decrease in SWS. This means that aerosols cool the surface more rapidly than the upper levels, reducing the vertical temperature gradient and stabilizing the lower atmosphere. During 2010–2020, the static stability of the lower-level PBL tends to be flat due to the aerosol reduction, which provides favorable conditions for increased SWS (Fig. 5b). This is consistent with the hypothesis that SWS generally decreases at plain stations but increases at neighboring hilltop stations (Yang et al. 2013). This difference reaches the largest around noon with stronger aerosol radiative effects, indicating trends of stabilization within the PBL and instability above the PBL.

The mean altitude of the meteorological stations in Northeast China is 304.7 m (Fig. S1), which is close to 975 hPa

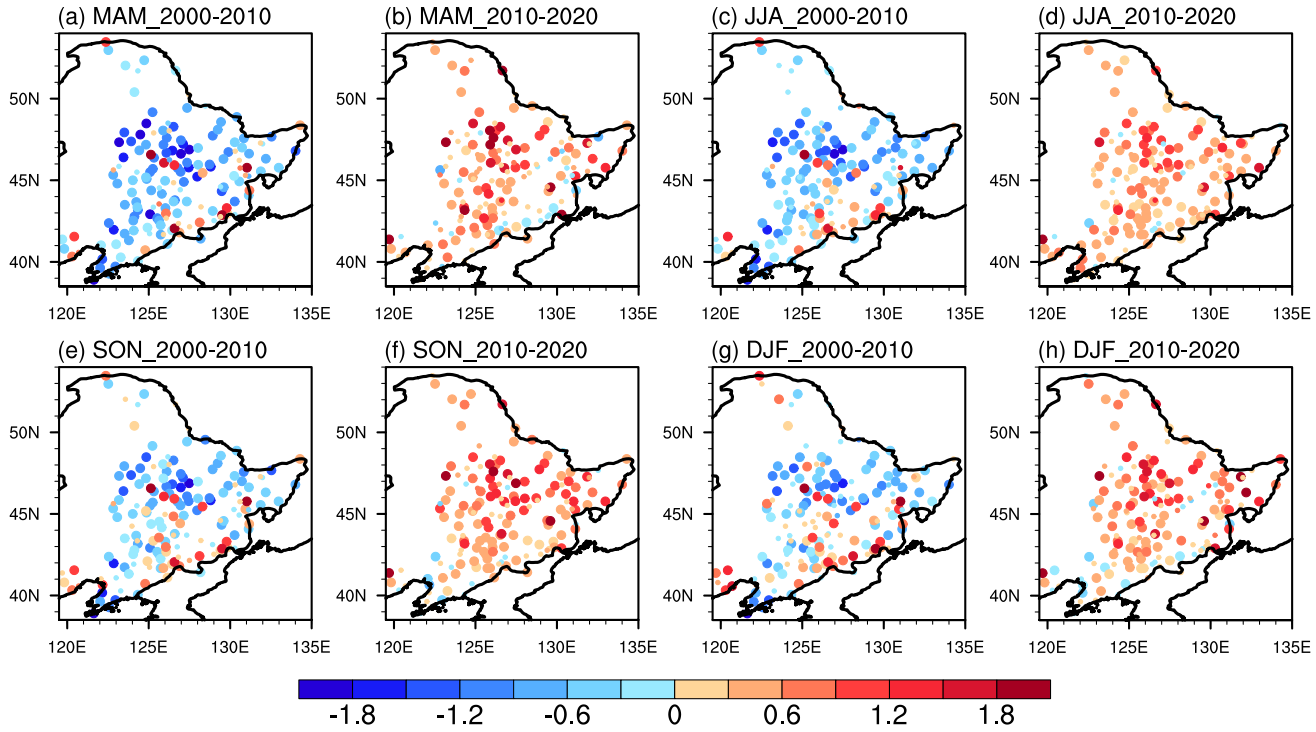

Fig. 3 Spatial patterns of linear trends in SWS (units: m s^{-1} per decade) in (**a** and **b**) spring, (**c** and **d**) summer, (**e** and **f**) autumn and (**g** and **h**) winter during the two periods of 2000–2010 (**a, c, e** and **g**) and 2010–2020 (**b, d, f** and **h**) are shown. Larger dots indicate the 90% confidence level (i.e., $P < 0.1$)

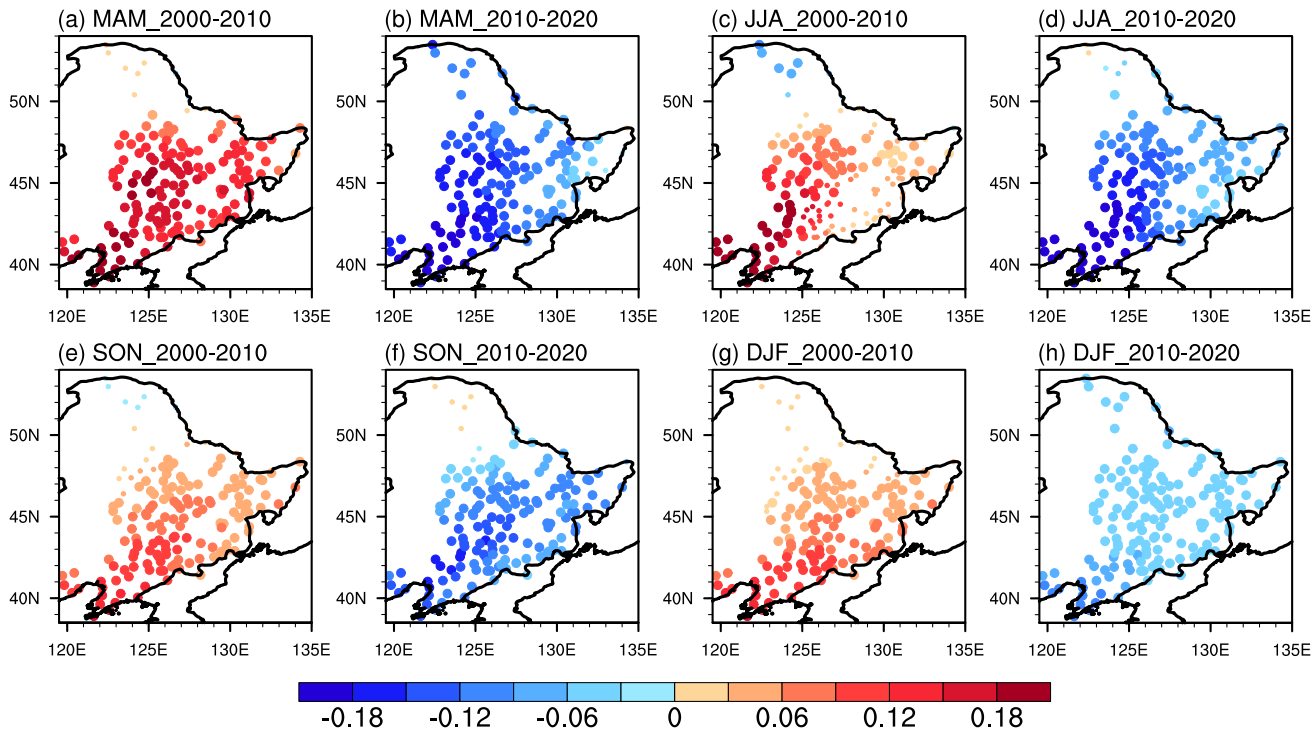

Fig. 4 Same as Fig. 3, but for spatial patterns of linear trends in AOD (units: per decade). Larger dots indicate the 90% confidence level (i.e., $P < 0.1$)

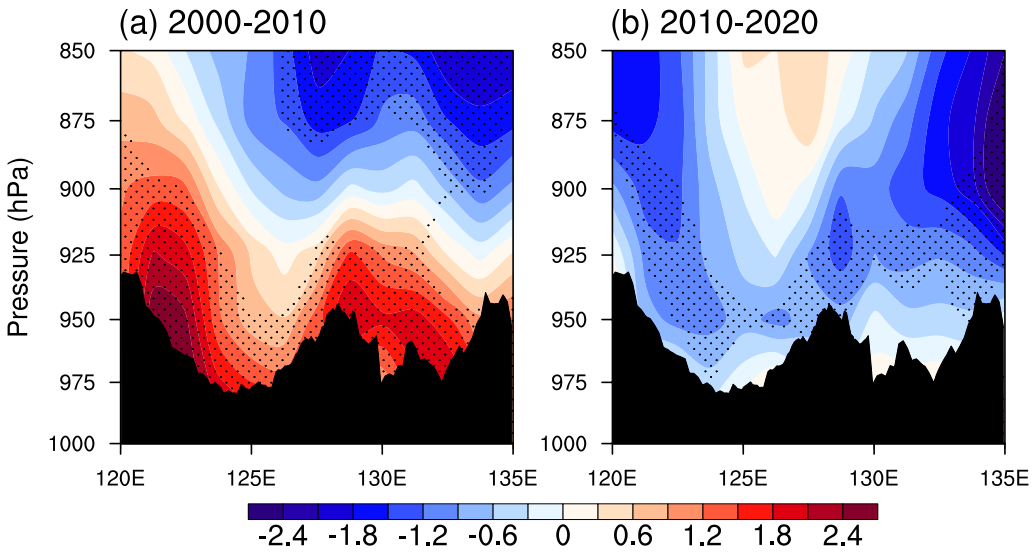

Fig. 5 Spatial patterns of linear trends in meridionally averaged static stability (units: 10^{-5} K Pa^{-1} per decade) between 38.5°N and 54°N during the periods of (**a**) 2000–2010 and (**b**) 2010–2020. Stippling indicates the significant trend exceeding the 90% confidence level ($P < 0.1$). Topography is indicated by black shading

(about 320 m). To further quantify and understand the relative changes associated with static stability transition, we show the time series of SWS and static stability at 975 hPa (the closest to site-mean altitude) in Fig. 6a. The interdecadal static stability exhibits a sharp fluctuating upward trend from 1980 to 2010, and flattens out after 2010. The correlation coefficient between SWS and static stability is −0.98 ($P < 0.001$), revealing that interdecadal variation of static stability is the main cause for the SWS reversal. Since TKE is not given in the JRA-55, Fig. 6b uses CFSR data to verify the relationship between SWS and TKE evolutions in Northeast China, which show a highly correlation with a correlation coefficient of 0.92 ($P < 0.001$). This suggests that the increase of static stability induced by increasing aerosols acts to suppress TKE production, consistent with the finding that lower AOD contributes to PBL turbulence growth (Grabowski et al. 2015; Jiang et al. 2002). The weakening of turbulence reduces vertical mixing, which in turn reduces the vertical flux of horizontal momentum. Since winds aloft are typically stronger than those near the surface, the

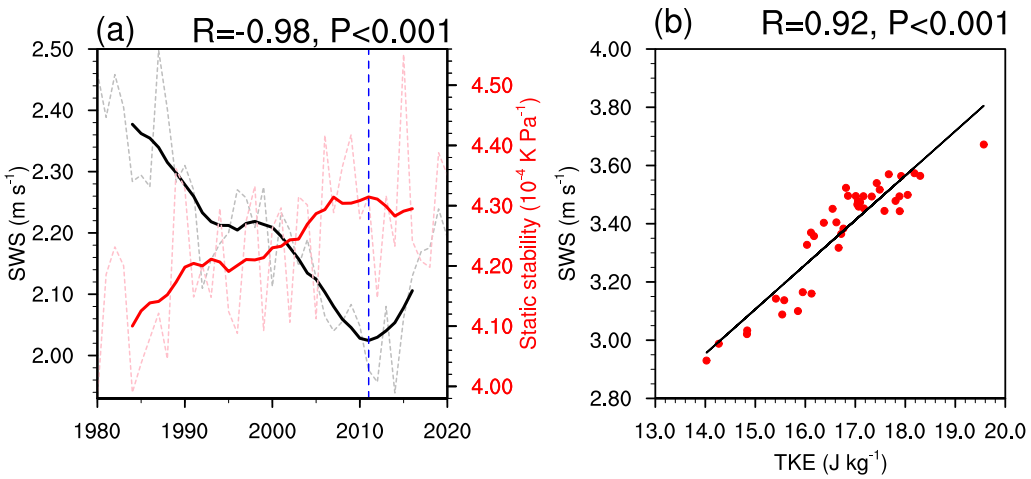

Fig. 6 **a** Time series of raw (light dashed curve) and 9-year Gaussian low-pass filtered (heavy solid curve) SWS (black; units: m s^{-1}) and static stability at 975 hPa (red; units: 10^{-4} K Pa^{-1}) in JRA-55 in Northeast China from 1980 to 2020. The vertical dashed blue lines denote the turning point. The significance of the correlation coefficient is based on an effective degree of freedom of 13.67 (**b**) The statistically significant relationship between time series of raw SWS (units: m s^{-1}) and TKE (units: J kg^{-1}) in CFSR in Northeast China from 1980 to 2020

weakened vertical mixing reduces the transmission of fast winds aloft to the surface, thus slowing down SWS.

4 Modeling results

4.1 Individual effect under different anthropogenic aerosol emission conditions simulated by CAM5.3 model

Based on the above analysis, we investigate the atmospheric responses in the PBL when anthropogenic aerosol emissions decrease in Northeast China using two sets of experiments from CAM5.3 model. Fig. S7 compares the simulated 10-year mean SWS in CTRL with the mean observed data (remapped onto the same grid as CAM5.3) from 1996 to 2005. It can be clearly seen that CTRL run well captures the geographical distribution of climatological mean SWS in Northeast China. The deviation of CAM5.3 from the observed SWS is generally small, although there is some underestimation in the eastern region and some overestimation in the Liaodong Peninsula.

Figure 7a–c show the distribution of SWS in Northeast China in the two experiments and their differences. In CTRL

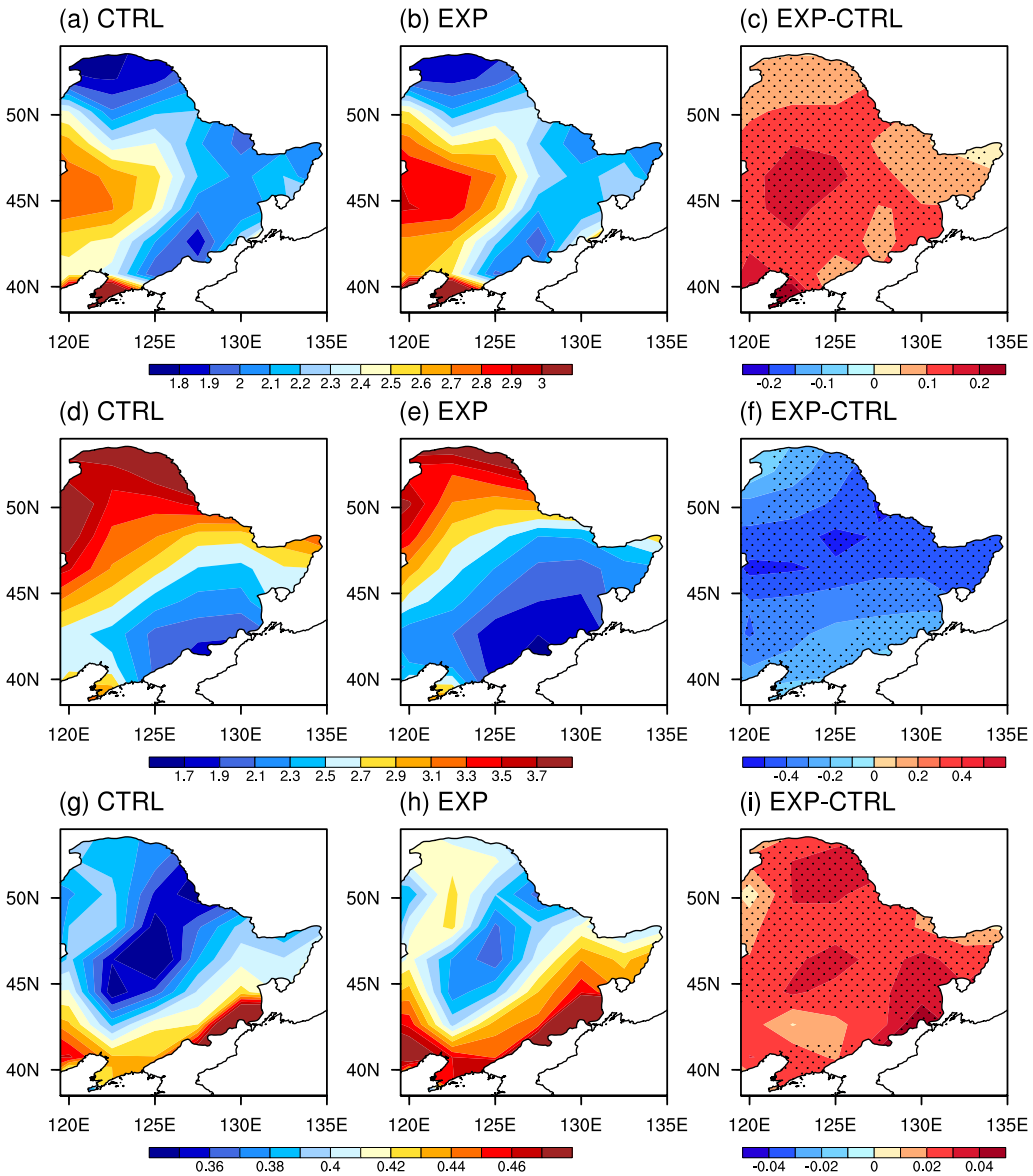

Fig. 7 Spatial patterns of simulated 10-year mean SWS (**a** and **b**; units: m s^{-1}), static stability (**d** and **e**; units: 10^{-4} K Pa^{-1}) at 975 hPa, wind gusts from turbulence (**g** and **h**; units: m s^{-1}) based on (**a**, **d**, and **g**) CTRL and (**b**, **e**, and **h**) the average of five EXP experiments and (**c**, **f**, and **i**) their differences (i.e., EXP minus CTRL) by CAM 5.3 model over Northeast China. Stippling in (**c**, **f**, and **i**) indicates the significant changes exceeding the 90% confidence level ($P < 0.1$)

and EXP experiments, the largest SWS is concentrated in the western part of Northeast China and also Liaodong Peninsula, while the smallest SWS is located in the northern mountainous region. When anthropogenic aerosols are dramatically reduced, SWS prominently increases by 0.05 to 0.2 m s^{-1} in most areas of Northeast China (Fig. 7c). The largest SWS increase (exceeding 0.2 m s^{-1}) is located in the Liaodong Peninsula, which is consistent with the location of the most significant changes in AOD trends (Fig. 2c, d). In addition, the spatial patterns of SWS in these two experiments are similar, indicating that regional anthropogenic aerosol emission reductions might not reshape the SWS pattern over Northeast China.

The static stability also shows a similar pattern in CTRL and EXP experiments, with the large value in the northwest and the small value in the southeast (Fig. 7d, e). As in observations, a substantial reduction in anthropogenic aerosol emissions can reduce the surface static stability (Fig. 7f), corresponding to the SWS increase. Surface wind gusts are caused by the deflection of air parcels flowing higher in the PBL, which can be attributed to vertical mixing by turbulent eddies (Brasseur 2001). Wind gusts from turbulence are larger in the southern part of Northeast China (Fig. 7g, h), and the positive changes of wind gusts are shown in Fig. 7i when anthropogenic aerosol emissions are reduced. An unstable layer favors the vertical transport, and air parcels responsible for the stronger gusts are deflected from nearly the top of the PBL. Meanwhile, when the PBL is unstable, a maximum of TKE generally reaches in the lowest part of the PBL (Lenschow et al. 1980), thus more conducive to the enhancement of surface winds. Thus, our simulation results further confirm the notion that the reduction of aerosol emissions can significantly increase SWS over Northeast China through weakening the surface static stability and strengthening TKE.

The PBL height, which indicates the degree of vertical mixing and exchange (Seidel et al. 2010), is significantly enhanced by reduced anthropogenic aerosol emissions (Fig. 8a–c). In general, a deeper boundary layer corresponds to more intense vertical turbulent mixing, which tends to reduce near-surface concentration of aerosols. The positive feedback between PBL and aerosol radiative forcing further enhances aerosol loading. Aerosol particles impact on the PBL properties through absorbing and scattering shortwave and longwave radiation. Clear-sky net shortwave radiation is greater in the southern region of Northeast China than in the northern region (Fig. 8d, e). With fewer aerosols, the amount of clear-sky net shortwave radiation reaching the surface increases (Fig. 8f), and the reduced absorption of radiation by fewer aerosol particles enhances vertical transport, thus making the atmosphere more unstable and enhancing low-level upward motion. The clear-sky net long-wave radiation decreases from southwest to northeast (Fig. 8g, h), and it is reduced by a decrease in aerosols (Fig. 8i), contrary to Fig. 8f, with a cooling effect that partially offsets the surface warming due to enhanced shortwave radiation. Aerosols also have an impact on the surface energy budget. The net surface heat flux is the sum of the net shortwave and longwave fluxes, and also sensible and latent heat fluxes at the surface, which is in response to aerosol radiative forcing. The simulation results show that the pattern of net surface heat flux is similar to that of clear-sky net shortwave radiation (Fig. 8j, k), because the latter accounts for the largest proportion of the former. Reduced aerosols induce a general increase of the net surface heat flux (Fig. 8l), resulting in a radiative heating near the surface. Meanwhile, the diminished absorption of solar energy by aerosols causes an atmospheric radiative cooling within the PBL, and as a consequence, this difference in temperature gradient leads to an increase in SWS.

4.2 Individual effect and quantitative contribution of AER, GHG and NAT forcing simulated by CMIP6 models

The DAMIP has been widely used to reveal the factors inducing long-term variability in various variables (Shen et al. 2021; Zhang et al. 2024). The potential effects of AOD in causing SWS changes are detected using numerical simulations from eight DAMIP models of the CMIP6. Figure 9 shows temporal evolutions of SWS, AOD, and static stability at 1000 hPa in AER experiment. The changes in AOD are highly consistent across all the models, with a sharp increase since 1940 due to rapid industrialization and urbanization. AOD peaks in 2010 and has been declining dramatically since then as the consequence of clean air actions, which is the same as the observations. We calculate the regional mean static stability at 1000 hPa (closest to the mean terrain height in Northeast China). The static stability of all the models, except for MIROC6 and NorESM2-LM, peaks in 2010 and then decreases, which is similar to the evolution of the AOD. The positive correlation between static stability and the AOD in the MME reaches 0.92 ($P < 0.001$). SWS shows no significant trend during 1900–1970, while it decreases significantly from 1970 to 2010 and increases after 2010 in the MME. The correlation coefficients of SWS with AOD and static stability in the MME are −0.95 ($P < 0.001$) and −0.92 ($P < 0.001$), respectively. This confirms the observational result that increasing AOD weakens SWS by increasing surface static stability.

Figure 10a–i display the temporal variations of SWS under different forcing factors. In AER experiment, the decreasing trend in SWS is most pronounced during 1970–2010 among three forcing factors. In GHG experiment, the MME result shows fluctuating downward trends in SWS during 1970–2020. This confirms that global warming generally leads to a decrease in SWS

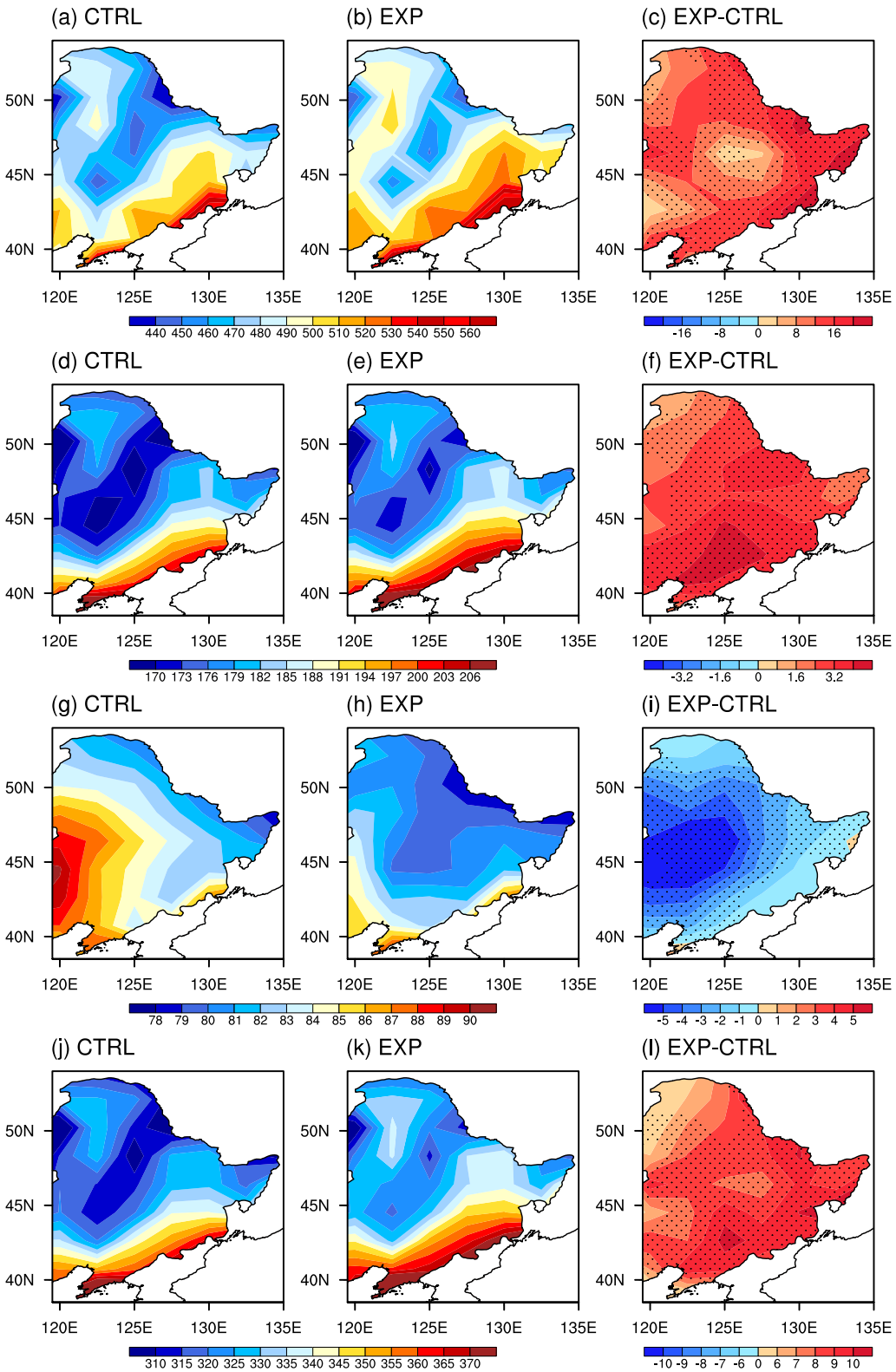

Fig. 8 Same as Fig. 7, but for the PBL height (**a**–**c**; units: m), clear-sky net shortwave flux at the surface (**d**–**f**; units: W m^{-2}), clear-sky net longwave flux at the surface (**g**–**i**; units: W m^{-2}), and net surface heat flux (**j**–**l**; units: W m^{-2}). Note that downwelling flux is positive. Stippling in (**c**, **f**, **i**, and **l**) indicates the significant changes exceeding the 90% confidence level ($P < 0.1$)

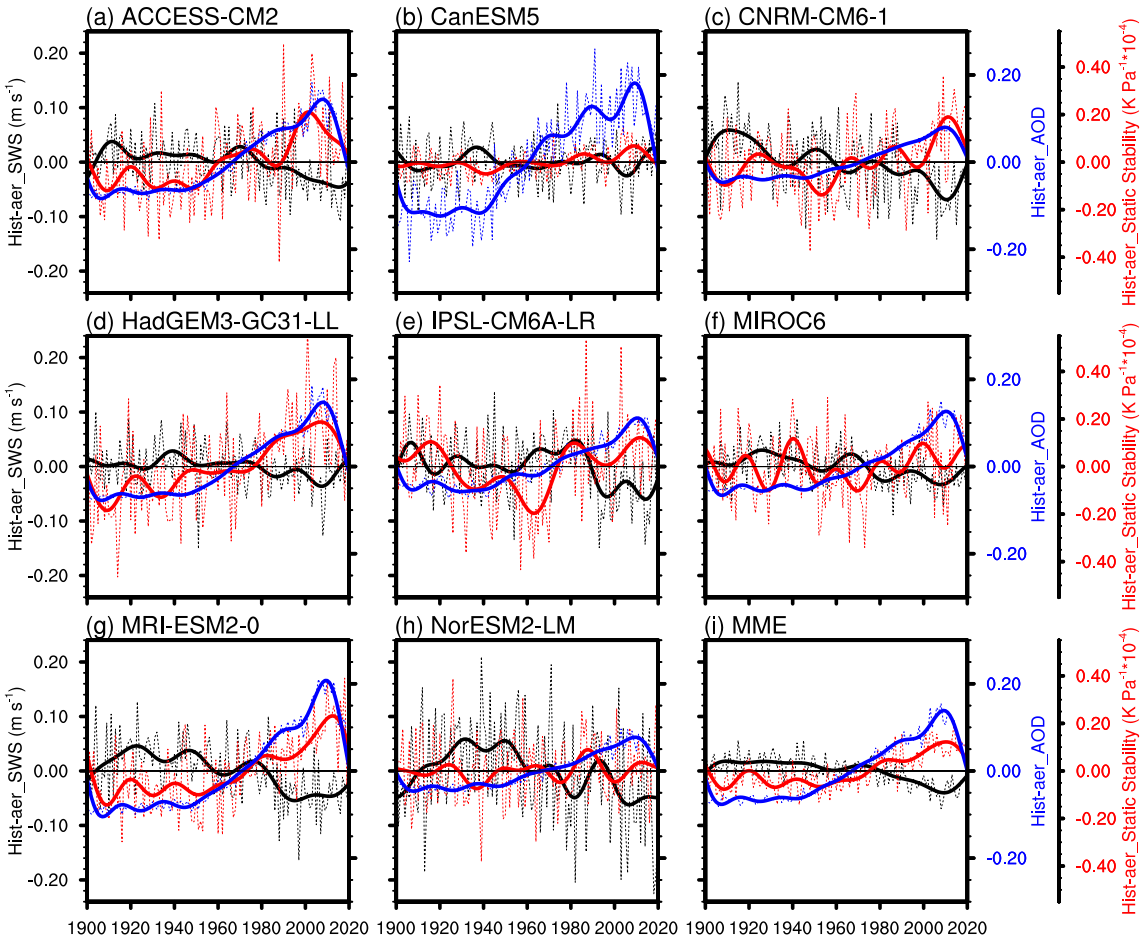

Fig. 9 Time series of raw (dashed curve) and 21-year Fourier low-pass filtered (solid curve) anomalies in SWS (black; units: m s^{-1}), AOD (blue), and static stability at 1000 hPa (red; units: 10^{-4} K Pa^{-1}) in the hist-aer (AER) simulation from eight CMIP6 models (**a**–**h**) and their MME (**i**) during 1900–2020. Each variable is calculated as a regional average for the study area (38.5°N–54°N, 119.5°E–135°E)

over the Northern Hemisphere (Zha et al. 2021a), where the Hadley, Ferrell, and Polar cells may be inhibited by substantial GHG warming. However, in NAT experiment, there is no significant trend change in SWS in each model over the whole period of 1900–2020. Using the multiple linear regression method described in Sect. 2.2.4, we obtain attributable trends in SWS over 1980–2010 and 2010–2020 (Fig. 10j, k). Results show that the observed decrease and increase in SWS over Northeast China can be largely explained by the influence of aerosols on the basis of the MME responses. During 1980–2010, the aerosol-induced SWS trend is −0.19 m s^{-1} per decade, accounting for 89.6% of the total observed trend. During 2010–2020, the increasing SWS trend caused by aerosols (0.50 m s^{-1} per decade) even exceeds the observed trend (0.47 m s^{-1} per decade). However, the influences of GHG and NAT are much weaker over the two periods.

5 Conclusions and discussion

The interdecadal change of SWS over Northeast China is featured by a reversal in 2010, which is different to time of SWS reversal over other regions of China. In this study, we propose a new factor of SWS reversal in Northeast China, which is the interdecadal variation of local aerosols. The interdecadal variations of both annual and seasonal mean SWS exhibit a decline during 1980–2010, followed by an increasing trend after 2010, which are linked to the interdecadal transition of aerosol emissions. AOD peaks in 2010 and then declines rapidly, showing a significant negative correlation with SWS, especially for the annual mean as well as spring and summer. Aerosols in other regions of eastern China also show a reversal of trend around 2010. However, aerosol change in these regions can't lead to a

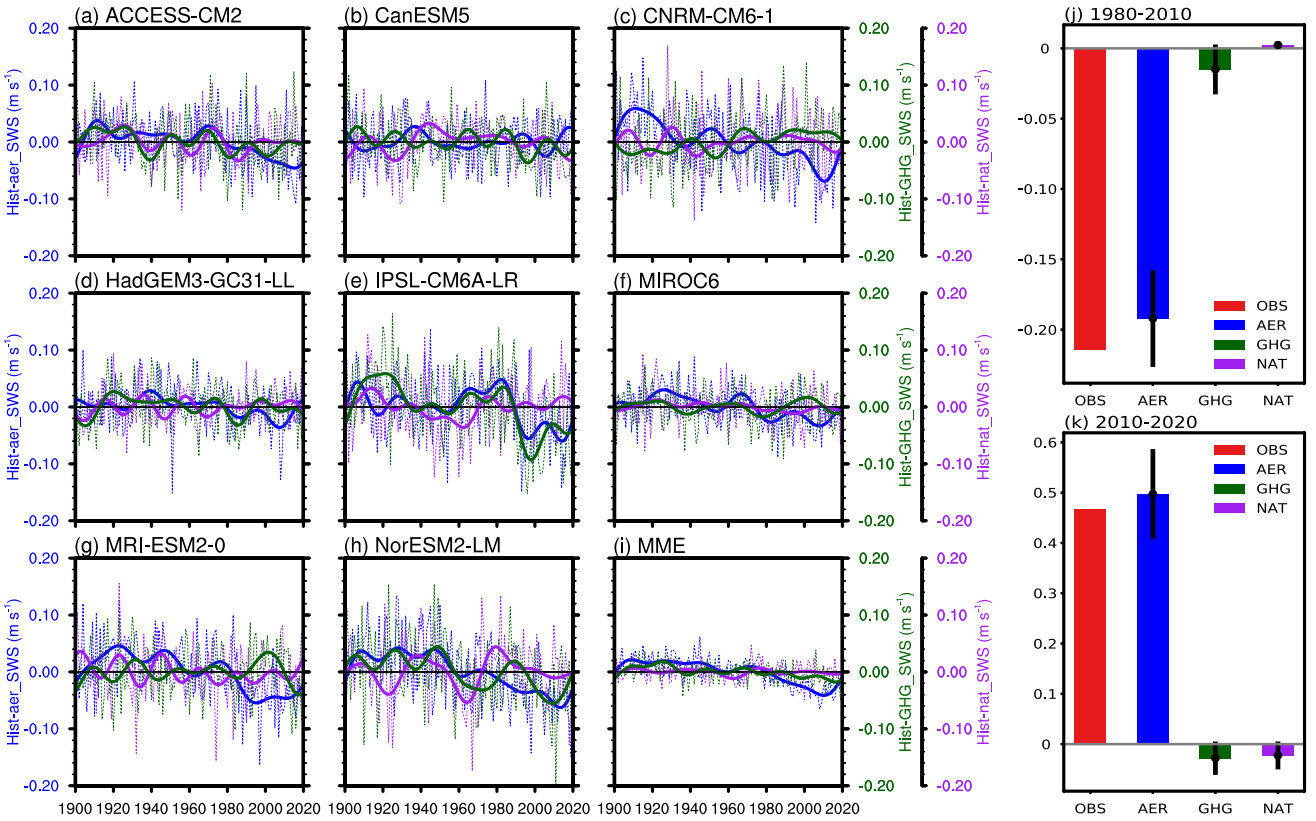

Fig. 10 Time series of raw (dashed curve) and 21-year Fourier low-pass filtered (solid curve) SWS anomalies (units: m s^{-1}) in hist-aer (AER, blue), hist-GHG (GHG, green) and hist-nat (NAT, purple) simulations from eight CMIP6 models (**a**–**h**) and their MME (**i**) during 1900–2020. Linear trends of SWS (units: m s^{-1} per decade) in the observations (red) and in AER (blue), GHG (green), and NAT (purple) simulations from CMIP6 MME during 1980–2010 (**j**) and 2010–2020 (**k**) based on the multiple linear regression model. The error bars denote the 95% confidence levels of simulated regional mean trends. Each variable is calculated as a regional average for the study area (38.5°N–54°N, 119.5°E–135°E)

reversal of SWS locally like in Northeast China, which suggests that aerosol plays a more important role in the change of SWS trend in Northeast China. Such a close connection between AOD and SWS in Northeast China is caused by aerosol-induced changes in the lower-level static stability. The aerosol reduction favors the development of instability and promotes the TKE growth and thus the increase of SWS. CAM5.3 outputs confirm that SWS will increase significantly by substantially reducing anthropogenic aerosol emissions in Northeast China and shed light on the impact processes and mechanisms. Reduced absorption of shortwave radiation by fewer aerosol particles results in surface warming and stronger vertical turbulent mixing, thus making the low-level atmosphere more unstable and strengthening local SWS. The result is further verified by multiple single forcing experiments in the DAMIP. In the aerosol forcing only experiment, the SWS decreases with the increasing AOD and surface static stability from 1970 to 2010 and strengthens after 2010 due to decreasing aerosol emissions. The decrease in SWS from 1970 to 2010 is caused by combined effects of aerosols and greenhouse warming, with a stronger impact from the former. The contribution of natural forcing to the change of SWS trend during 1900–2020 is little. Quantitative estimate indicates that the anthropogenic aerosol reduction is the dominant contributor to the increasing SWS observed in the recent decade over Northeast China. These findings highlight the crucial role of reducing aerosol emissions in mitigating the energy crisis and sustainable development of human society.

Previous studies have emphasized the influence of PDO and NAO, etc. on the changes of SWS in large regions (e.g., East Asia or eastern China, Zeng et al. 2019; Li et al. 2022), but we found that the changes of upper atmospheric circulation in Northeast China are not closely related to PDO and NAO. In this study, we show that the aerosol radiation effects can locally increase the atmospheric stability and convective potential of the lower atmosphere, leading to lower temperatures and weaker winds. The atmospheric stabilization affects turbulence and vertical transport of horizontal momentum, causing different changes of SWS and local circulation at the high and low

altitudes. In addition, on the continental scale, aerosols absorb solar radiation and cool the surface, which can reduce the land–ocean thermal contrast to suppress the monsoon development (Lau et al. 2016). As the Asian monsoon region is a major source of various aerosol emissions, the aerosol-induced SWS reduction is more intense in East Asia and South Asia than in the other regions (Li et al. 2016). As a result, the influence of aerosols on SWS is expected to be closely related to that on the monsoon circulation. However, the underlying physical mechanism is complex and should be investigated more systematically in the future. Note that GHG warming is also found to trigger the SWS trend (Fig. 10), which appears to be through its modulation of the meridional atmospheric circulation (Deng et al. 2021).

Regarding future projections in SWS in China, Miao et al. (2023) found a nonlinear relation that SWS would decrease most sharply under the SSP3-7.0 scenario rather than the highest GHG emission scenario (SSP5-8.5). This is mainly due to the fact that the SSP3-7.0 scenario represents much higher aerosol emissions than the other scenarios, mainly consisting of black carbon and sulfate aerosols (Chen et al. 2020; Riahi et al. 2017). Previous studies have also mentioned some other unique climate impacts of the SSP3-7.0 scenario in China. This scenario will lead to a significant decline in yield over Northeast China due to reduced solar radiation and precipitation (Zhang et al. 2023). In addition, compared to the other three scenarios (SSP1-2.6, SSP2-4.5, and SSP5-8.5), the SSP3-7.0 scenario will bring the most severe future drought in China (Chen et al. 2021). The highest emissions of SO_2, N_2O, and CH_4 in SSP3-7.0 result in extensive climate damages and negative economic impacts. This study can further provide decision support and policy recommendations for sustainable development, that is, active air pollution control can be beneficial in curbing the reduction of wind energy in Northeast China under future climate change.

Supplementary Information The online version contains supplementary material available at https://doi.org/10.1007/s00382-024-07544-0.

Acknowledgements This work is supported by the National Natural Science Foundation of China (Grants 42192562, 41975106, and 42105032). We thank the High Performance Computing Center of Nanjing University of Information Science & Technology for supporting this research. Gratitude is extended to all the institutions for providing the relevant data used in this study.

Author contributions HM, HX, and GH conceived the study, designed the methodology and built the mechanisms. HM performed the formal analyses, made the figures and wrote the draft manuscript. HX formulated the main ideas, contributed to the design of the analyses, and helped review and editing the manuscript. KY, HT, JD, MX, GN and GH contributed to improving the manuscript and assisted in the interpretation of the results. All authors read and approved the final manuscript.

Funding This work is supported by the National Natural Science Foundation of China (Grants 42192562, 41975106, and 42105032).

Data availability Observational surface wind speeds used in this study from the daily dataset of basic meteorological elements of China's national ground meteorological stations (V3.0) can be obtained at http://data.cma.cn/data/cdcdetail/dataCode/A.0012.0001.html supported by the China Meteorological Data Service Center. The MERRA-2 dataset is from the National Aeronautics and Space Administration Goddard Space Flight Center (NASA/GSFC): https://disc.gsfc.nasa.gov/datasets?project=MERRA-2. The ERA-5 reanalysis data is available at https://cds.climate.copernicus.eu/cdsapp#!/dataset/reanalysis-era5-single-levels-monthly-means?tab=form from the European Centre for Medium-Range Weather Forecasts (ECMWF). The JRA-55 dataset is at https://jra.kishou.go.jp/JRA-55/index_en.html from the Japan Meteorological Agency (JMA). The CFSR data is acquired from the NCAR Research Data Archive (RDA) (https://rda.ucar.edu/datasets/ds093.0/dataaccess/#). The CMIP6 outputs used in this study can be downloaded from https://esgf-node.llnl.gov/projects/cmip6/. The CESM1 model is available from https://doi.org/https://doi.org/10.26024/rn3t-ep30.

Declarations

Conflict of interests The authors have no relevant financial or non-financial interests to disclose.

References

Bichet A, Wild M, Folini D, Schär C (2012) Causes for decadal variations of wind speed over land: sensitivity studies with a global climate model. Geophys Res Lett 39:L11701. https://doi.org/10.1029/2012GL051685

Bluestein HB (1992) Synoptic-dynamic meteorology in midlatitudes: principles of kinematics and dynamics. Oxford University Press, New York, p 276

Brasseur O (2001) Development and application of a physical approach to estimating wind gusts. Mon Wea Rev 129:5–25. https://doi.org/10.1175/1520-0493(2001)129%3c0005:DAAOAP%3e2.0.CO;2

Chen Y, Liu A, Cheng X (2020) Quantifying economic impacts of climate change under nine future emission scenarios within CMIP6. Sci Total Environ 703:134950. https://doi.org/10.1016/j.scitotenv.2019.134950

Chen L, Wang G, Miao L, Gnyawali KR, Li S, Amankwah SOY, Huang J, Lu J, Zhan M (2021) Future drought in CMIP6 projections and the socioeconomic impacts in China. Int J Climatol 41:4151–4170. https://doi.org/10.1002/joc.7064

Deng J, Xu H (2015) Atmospheric responses to idealized urban land surface forcing in eastern China during the boreal spring. J Geophys Res Atmos 120:10022–10039. https://doi.org/10.1002/2015JD023748

Deng K, Azorin-Molina C, Minola L, Zhang G, Chen D (2021) Global near-surface wind speed changes over the last decades revealed by reanalyses and CMIP6 model simulations. J Clim 34:2219–2234. https://doi.org/10.1175/JCLI-D-20-0310.1

Ding AJ, Huang X, Nie W, Sun JN et al (2016) Enhanced haze pollution by black carbon in megacities in China. Geophys Res Lett 43:2873–2879. https://doi.org/10.1002/2016GL067745

Gelaro R, McCarty W, Suárez MJ, Todling R et al (2017) The modern-era retrospective analysis for research and applications, version 2 (MERRA-2). J Clim 30:5419–5454. https://doi.org/10.1175/JCLI-D-16-0758.1

Gillett NP, Shiogama H, Funke B, Hegerl G, Knutti R, Matthes K, Santer BD, Stone D, Tebaldi C (2016) Detection and attribution model intercomparison project (DAMIP). Geosci Model Dev 9:3685–3697. https://doi.org/10.5194/gmd-2016-74

Grabowski WW, Wang LP, Prabha TV (2015) Macroscopic impacts of cloud and precipitation processes on maritime shallow convection as simulated by a large eddy simulation model with bin microphysics. Atmos Chem Phys 15:913–926. https://doi.org/10.5194/acp-15-913-2015

Guo H, Xu M, Hu Q (2011) Changes in near-surface wind speed in China: 1969–2005. Int J Climatol 31:349–358. https://doi.org/10.1002/joc.2091

He Q, Li C, Geng F, Lei Y, Li Y (2012) Study on long-term aerosol distribution over the land of East China using MODIS data. Aerosol Air Qual Res 12:304–319. https://doi.org/10.5194/acpd-11-10485-2011

Hersbach H, Bell B, Berrisford P, Hirahara S et al (2020) The ERA5 global reanalysis. Q J R Meteorol Soc 146:1999–2049. https://doi.org/10.1002/qj.3803

Jacobson MZ, Kaufman YJ (2006) Wind reduction by aerosol particles. Geophys Res Lett 33:L24814. https://doi.org/10.1029/2006GL027838

Jiang H, Feingold G, Cotton WR (2002) Simulations of aerosol-cloud-dynamical feedbacks resulting from entrainment of aerosol into the marine boundary layer during the Atlantic Stratocumulus Transition Experiment. J Geophys Res Atmos 107:24. https://doi.org/10.1029/2001JD001502

Jiang Q, Li W, Fan Z, He X, Sun W, Chen S, Wen J, Gao J, Wang J (2021) Evaluation of the ERA5 reanalysis precipitation dataset over Chinese Mainland. J Hydrol 595:125660. https://doi.org/10.1016/j.jhydrol.2020.125660

Kobayashi S, Ota Y, Harada Y, Ebita A et al (2015) The JRA-55 reanalysis: General specifications and basic characteristics. J Meteorol Soc Jpn Ser II 93:5–48. https://doi.org/10.2151/jmsj.2015-001

Lau WK (2016) The aerosol-monsoon climate system of Asia: a new paradigm. J Meteorol Res 30:1–11. https://doi.org/10.1007/s13351-015-5999-1

Lenschow DH, Wyngaard JC, Pennell WT (1980) Mean-field and second-moment budgets in a baroclinic, convective boundary layer. J Atmos Sci 37:1313–1326

Li Z, Niu F, Fan J, Liu Y, Rosenfeld D, Ding Y (2011) Long-term impacts of aerosols on the vertical development of clouds and precipitation. Nat Geosci 4:888–894. https://doi.org/10.1038/ngeo1313

Li Z, Lau WM, Ramanathan V, Wu G (2016) Aerosol and monsoon climate interactions over Asia. Rev Geophys 54:866–929. https://doi.org/10.1002/2015RG000500

Li Z, Song L, Ma H, Xiao J, Wang K, Chen L (2018) Observed surface wind speed declining induced by urbanization in East China. Clim Dyn 50:735–749. https://doi.org/10.1007/s00382-017-3637-6

Li X, Li QP, Ding YH, Wang M (2022) Near-surface wind speed changes in eastern China during 1970–2019 winter and its possible causes. Adv Clim Change Res 13:228–239. https://doi.org/10.1016/j.accre.2022.01.003

Lin C, Yang K, Qin J, Fu R (2013) Observed coherent trends of surface and upper-air wind speed over China since 1960. J Clim 26:2891–2903. https://doi.org/10.1175/JCLI-D-12-00093.1

McVicar TR, Roderick ML, Donohue RJ, Li LT et al (2012) Global review and synthesis of trends in observed terrestrial near-surface wind speeds: implications for evaporation. J Hydrol 416:182–205. https://doi.org/10.1016/j.jhydrol.2011.10.024

Miao H, Dong D, Huang G, Hu K, Tian Q, Gong Y (2020) Evaluation of Northern Hemisphere surface wind speed and wind power density in multiple reanalysis datasets. Energy 200:117382. https://doi.org/10.1016/j.energy.2020.117382

Miao H, Xu H, Huang G, Yang K (2023) Evaluation and future projections of wind energy resources over the Northern Hemisphere in CMIP5 and CMIP6 models. Renew Energy 211:809–821. https://doi.org/10.1016/j.renene.2023.05.007

Moreira EE, Martins DS, Pereira LS (2015) Assessing drought cycles in SPI time series using a Fourier analysis. Nat Hazards Earth Syst Sci 15:571–585. https://doi.org/10.5194/nhess-15-571-2015

Neale RB, Chen CC, Gettelman A, Lauritzen PH (2010) Description of the NCAR Community Atmosphere Model (CAM5.0). http://www.cesm.ucar.edu/models/cesm1.0/cam/docs/description/cam5_desc.pdf

Paulot F, Naik V, Horowitz W, L, (2022) Reduction in near-surface wind speeds with increasing CO_2 may worsen winter air quality in the indo-gangetic plain. Geophys Res Lett 49:e2022GL099039. https://doi.org/10.1029/2022GL099039

Pettitt AN (1979) A non-parametric approach to the change-point problem. J R Stat Soc Ser C 28:126–135. https://doi.org/10.2307/2346729

Riahi K, Van Vuuren DP, Kriegler E, Edmonds J (2017) The Shared Socioeconomic Pathways and their energy, land use, and greenhouse gas emissions implications: an overview. Glob Environ Change 42:153–168. https://doi.org/10.1016/j.gloenvcha.2016.05.009

Saha S, Moorthi S, Pan HL, Wu X (2010) The NCEP climate forecast system reanalysis. Bull Am Meteorol Soc 91:1015–1058. https://doi.org/10.1175/2010BAMS3001.1

Schaefer D, Domroes M (2009) Recent climate change in Japan-spatial and temporal characteristics of trends of temperature. Clim past 5:13–19. https://doi.org/10.5194/cp-5-13-2009

Seidel DJ, Ao CO, Li K (2010) Estimating climatological planetary boundary layer heights from radiosonde observations: comparison of methods and uncertainty analysis. J Geophys Res 115:D16. https://doi.org/10.1029/2009jd013680

Sen PK (1968) Estimates of the regression coefficient based on Kendall's tau. J Am Stat Assoc 63:1379–1389. https://doi.org/10.1080/01621459.1968.10480934

Shen C, Zha J, Zhao D, Wu J, Fan W, Yang M, Li Z (2021) Estimating centennial-scale changes in global terrestrial near-surface wind speed based on CMIP6 GCMs. Environ Res Lett 16:084039. https://doi.org/10.1088/1748-9326/ac1378

Su T, Feng T, Feng G (2015) Evaporation variability under climate warming in five reanalyses and its association with pan evaporation over China. J Geophys Res Atmos 120:8080–8098. https://doi.org/10.1002/2014JD023040

Tariq S, Qayyum F, Ul-Haq Z, Mehmood U (2022) Long-term spatiotemporal trends in aerosol optical depth and its relationship with enhanced vegetation index and meteorological parameters over South Asia. Environ Sci Pollut Res 29:30638–30655. https://doi.org/10.1007/s11356-021-17887-4

Tian Q, Huang G, Hu K, Niyogi D (2019) Observed and global climate model based changes in wind power potential over the Northern Hemisphere during 1979–2016. Energy 167:1224–1235. https://doi.org/10.1016/j.energy.2018.11.027

Vautard R, Cattiaux J, Yiou P, Thépaut JN, Ciais P (2010) Northern Hemisphere atmospheric stilling partly attributed to an increase in surface roughness. Nat Geosci 3:756–761. https://doi.org/10.1038/ngeo979

Xu M, Chang CP, Fu C, Qi Y, Robock A, Robinson D, Zhang HM (2006) Steady decline of east Asian monsoon winds, 1969–2000: evidence from direct ground measurements of wind speed. J Geophys Res Atmos 111:D24. https://doi.org/10.1029/2006JD007337

Xu M, Xu H, Ma J, Deng J (2022) Impact of Pacific Decadal Oscillation on interannual relationship between El Niño and South China Sea summer monsoon onset. Int J Climatol 42:2739–2753. https://doi.org/10.1002/joc.7388

Yang X, Ferrat M, Li Z (2013) New evidence of orographic precipitation suppression by aerosols in central China. Meteorog Atmos Phys 119:17–29. https://doi.org/10.1007/s00703-012-0221-9

Yu H, Liu SC, Dickinson RE (2002) Radiative effects of aerosols on the evolution of the atmospheric boundary layer. J Geophys Res Atmos 107:4142. https://doi.org/10.1029/2001JD000754

Zeng Z, Ziegler AD, Searchinger T, Yang L et al (2019) A reversal in global terrestrial stilling and its implications for wind energy production. Nat Clim Chang 9:979–985. https://doi.org/10.1038/s41558-019-0622-6

Zha J, Wu J, Zhao D (2017) Effects of land use and cover change on the near-surface wind speed over China in the last 30 years. Progress Phys Geog Earth Environ 41:46–67. https://doi.org/10.1177/0309133316663097

Zha J, Shen C, Zhao D, Wu J, Fan W (2021b) Slowdown and reversal of terrestrial near-surface wind speed and its future changes over eastern China. Environ Res Lett 16:034028. https://doi.org/10.1088/1748-9326/abe2cd

Zha J, Shen C, Li Z, Wu J, Zhao D, Fan W, Sun M, Azorin-Molina C, Deng K (2021a) Projected changes in global terrestrial near-surface wind speed in 1.5°C–4.0°C global warming levels. Environ Res Lett 16:114016. https://doi.org/10.1088/1748-9326/ac2fdd

Zhang Z, Wang K (2020) Stilling and recovery of the surface wind speed based on observation, reanalysis, and geostrophic wind theory over China from 1960 to 2017. J Clim 33:3989–4008. https://doi.org/10.1175/JCLI-D-19-0281.1

Zhang Y, Liu H, Qi J, Fend P, Zhang X, Liu D, Marel GW, Srinivasan R, Chen Y (2023) Assessing impacts of global climate change on water and food security in the black soil region of Northeast China using an improved SWAT-CO2 model. Sci Total Environ 857:159482. https://doi.org/10.1016/j.scitotenv.2022.159482

Zhang J, Ren G, You Q (2024) Detection and attribution of human-perceived warming over China. Geophys Res Lett 51:e2023GL106283. https://doi.org/10.1029/2023GL106283

Zhou C, Liu P, Huang G, Lin J, Hu K, Chen L, Wang J, Li S, Wang S, Ni R (2020) The impact of secondary inorganic aerosol emissions change on surface air temperature in the Northern Hemisphere. Theor Appl Climatol 141:857–868. https://doi.org/10.1007/s00704-020-03249-6

Publisher's Note Springer Nature remains neutral with regard to jurisdictional claims in published maps and institutional affiliations.

Springer Nature or its licensor (e.g. a society or other partner) holds exclusive rights to this article under a publishing agreement with the author(s) or other rightsholder(s); author self-archiving of the accepted manuscript version of this article is solely governed by the terms of such publishing agreement and applicable law.